Method to observe Jupiter's radio emissions at high resolution using multiple LOFAR stations: a first case study of the Io-decametric emission using the Irish IE613, French FR606, and German DE604 stations

Corentin K. Louis, C. M. Jackman, Jean-Mathias Griessmeier, O. Wucknitz, D. J. Mckenna, P. C. Murphy, P. T. Gallagher, E. P. Carley, D. Ó Fionnagáin, A. Golden, et al.

RAS Techniques and Instruments

RASTAI **1,** 48–57 (2022) https://doi.org/10.1093/rasti/rzac005
Advance Access publication 2022 October 14

Method to observe Jupiter's radio emissions at high resolution using multiple LOFAR stations: a first case study of the Io-decametric emission using the Irish IE613, French FR606, and German DE604 stations

Corentin K. Louis [1,2★] C. M. Jackman [1] J.-M. Grießmeier [2,3] O. Wucknitz [4] D. J. McKenna [1,5] P. C. Murphy [1,5] P. T. Gallagher [1,5] E. P. Carley [1] D. Ó Fionnagáin [6] A. Golden [6,7] J. McCauley [5] P. Callanan [8] M. Redman [9] and C. Vocks [10]

[1]*School of Cosmic Physics, DIAS Dunsink Observatory, Dublin Institute for Advanced Studies, Dublin 15, Ireland*
[2]*Station de Radioastronomie de Nançay, Observatoire de Paris, PSL Research University, CNRS, Université d'Orléans, F-18330 Nançay, France*
[3]*LPC2E - Université d'Orléans/CNRS, 45071 Orléans, France*
[4]*Max-Planck-Institut für Radioastronomie, Auf dem Hügel 69, D-53121 Bonn, Germany*
[5]*School of Physics, Trinity College Dublin, Dublin, D02 PN40, Ireland*
[6]*Astrophysics Research Group, School of Mathematics, Statistics and Applied Mathematics, National University of Ireland Galway, University Road, Galway, H91 H3CY, Ireland*
[7]*Armagh Observatory and Planetarium, College Hill, Armagh, BT61 9DB, N. Ireland*
[8]*Department of Physics, University College Cork, Cork, T12 CY82, Ireland*
[9]*Centre for Astronomy, School of Physics, National University of Ireland Galway, University Road, Galway, H91 TK33, Ireland*
[10]*Leibniz-Institut für Astrophysik Potsdam (AIP), An der Sternwarte 16, D-14482 Potsdam, Germany*

Accepted 2022 September 2. Received 2022 July 22; in original form 2021 November 17

ABSTRACT

The Low Frequency Array (LOFAR) is an international radio telescope array, consisting of 38 stations in the Netherlands and 14 international stations spread over Europe. Here, we present an observation method to study the Jovian decametric radio emissions from several LOFAR stations (here Birr Castle in Ireland, Nançay in France, and Postdam in Germany), at high temporal and spectral resolution. This method is based on prediction tools, such as radio emission simulations and probability maps, and data processing. We report an observation of Io-induced decametric emission from 2021 June, and a first case study of the substructures that compose the macroscopic emissions (called millisecond bursts). The study of these bursts makes it possible to determine the electron populations at the origin of these emissions. We then present several possible future avenues for study based on these observations. The methodology and study perspectives described in this paper can be applied to new observations of Jovian radio emissions induced by Io, but also by Ganymede or Europa, or Jovian auroral radio emissions.

Key words: instrumentation: interferometers – methods: observational – planets and satellites: aurorae – planets and satellites: individual: Io – planets and satellites: individual: Jupiter.

1 INTRODUCTION

In our Solar system, Jupiter is the planet with the most intense radio emissions, covering the broadest frequency range from a few kHz (where quasi-periodic bursts are seen) up to 40 MHz (the decametric, or DAM, emissions). From the ground, only the DAM emissions are observable, as all other lower frequency radio emissions are blocked by the ionospheric cutoff at ∼10 MHz. These DAM radio emissions were discovered quite early by Burke & Franklin (1955). A few years later, Bigg (1964) discovered that part of the DAM emission was controlled by the interaction between Jupiter's magnetosphere and the Galilean moon Io. The DAM emissions are known to be generated by the electron cyclotron maser instability (CMI) in the Jovian magnetosphere, which occurs when a circularly polarized wave resonates with the gyration movement of electrons with relativistic energies (Twiss 1958; Hirshfield & Bekefi 1963; Wu & Lee 1979; Zarka 1998; Treumann 2006; Louarn et al. 2017; Louis et al. 2020c). The source regions of the DAM emission are located above the atmosphere, on magnetic field lines of magnetic apex (distance of the magnetic field lines at the magnetic equator) between 15 and 50 R_J (1 R_J = 71492 km the Jovian radius, Louis et al. 2019b). The CMI gives rise to emission at a frequency close to the local electron cyclotron frequency f_{ce} (between f_{ce} and ∼1 per cent above f_{ce}, Louarn et al. 2017), which is directly proportional to the magnetic field amplitude B:

$$f_{ce} = \frac{|q|B}{2\pi m_e} \quad (1)$$

with q and m_e the electronic charge and mass. The CMI emission is beamed along a hollow cone (with a thickness of ∼1°, Kaiser et al. 2000) at large angle with respect to the local magnetic field

★ E-mail: corentin.louis@dias.ie

line (from ∼75° up to 90°, Pritchett 1986; Louis et al. 2017c). From the observer's point of view, these emissions have an arc-shape in a time-frequency map (Marques et al. 2017).

Our knowledge on the CMI emissions allows us to simulate these arcs (Louis et al. 2019a), which makes it possible to retrieve the energy of the electrons that produce these emissions (Hess, Cecconi & Zarka 2008; Louis et al. 2017c), as well as discover new components, such as DAM emissions induced by the Galilean moons Europa and Ganymede (Louis et al. 2017b).

However, the physics of the substructures that compose these macroscopic emissions is less well known. Their study requires observations at high temporal and spectral resolution. Unfortunately, most instruments do not have sufficiently high resolution to make the required measurements. For instruments onboard space missions, the telemetry often requires reduced frequency and time resolution. For ground-based radio telescopes, high spatial resolution requires tied-array beam forming or interferometric measurements with a large number of antennas, but also the ability to store very large amounts of data. The latest generation of radio telescopes, such as Low Frequency Array (LOFAR; van Haarlem et al. 2013) or NenuFAR (Zarka et al. 2012, 2015), provides measurements at very high temporal and spectral resolution.

Only a few authors have looked at these millisecond micro-bursts that composed the arc-shape radio emission. Zarka et al. (1996) were able to observe these millisecond bursts of Io-DAM emission using the Nançay Decameter Array (NDA, Boischot et al. 1980) and the Ukrainian Decameter T-shaped Array Radio Telescope (Braude, Men & Sodin 1978) observatories, with time and spectral resolution of 10 ms and 13 kHz, respectively, as well as Hess, Zarka & Mottez (2007b) using only the NDA observatory with a time and frequency resolution of 3 ms and 50 kHz, respectively. These two studies showed that these millisecond bursts are due to electron bunches propagating along the magnetic field lines. Abrupt changes in the drift rate of these millisecond bursts can also reveal electric potential drops along these field lines that brutally accelerate the electrons. Hess, Mottez & Zarka (2007a) were able to model these millisecond bursts by assuming that electrons are accelerated by Alfvén waves in the Io flux tube. Zarka (2004) showed the feasibility to do fast radio imaging of Jupiter's magnetosphere at radio frequency using a single LOFAR station.

In this article, we show that the inclusion of the Irish extension of the LOFAR telescope (I-LOFAR) and the use of both simulations and improved probability maps can extend and enhance the observation of these millisecond structures. In the following, we present the methodology of our observations and a first observation taken in 2021 June.

2 METHODOLOGY

2.1 LOFAR stations

The LOFAR is an international radio telescope array (see Fig. 1), consisting of 38 stations in the Netherlands and 14 international stations spread over Europe. In this present study, the following stations are used: German DE604, French FR606, and Irish IE613 (highlighted in red Fig. 1).

At each LOFAR station, a backend is used to record and analyse the raw beam formed data in real-time. At the DE604 and FR606 stations, raw data packets were written to disc after lossless compression (using the *Zstandard* algorithm). At the IE613 station, the REAL-time Transient Acquisition (REALTA; Murphy et al. 2021) backend was used. Similar successes have already been achieved with these

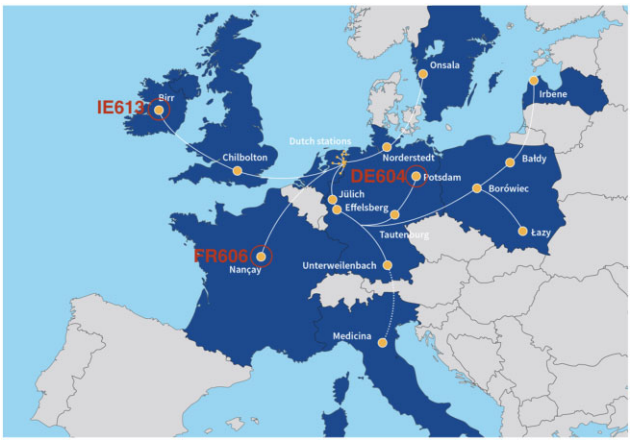

Figure 1. Map showing the location of LOFAR stations across Europe. 38 stations are located in the Netherlands, while 14 (soon 15) stations are located in seven (soon eight) other European countries. Here are highlighted the three stations that were used in the first case study described in Section 3: the Irish IE613, the French FR606, and the German DE604 stations.

different backends and used to conduct comparative studies (see e.g. Grießmeier et al. 2021). After data have been recorded to disc, *digifil* (as part of the *dspsr* package; van Straten & Bailes 2011) was used at all stations to generate the antenna auto-correlation and cross-correlation factors between both (perpendicular) linear polarization directions X and Y, from the underlying voltage data. Finally, a Jovian emission processing pipeline (Louis 2022) was run to retrieve the full Stokes parameters from the antenna autocorrelation and cross-correlation factors.

For the study of the Jovian DAM radio emissions (extending up to 40 MHz), only the LOFAR low-band antenna is used, which allows to make observations in the 8–90 MHz frequency range, with a temporal sampling interval that can go down to 5 ns.

2.2 Optimal observation conditions

To be able to observe Jupiter's radio emissions in the best possible conditions, the ionosphere should be in a quiet state to avoid supplementary interference, thus during night when the ionosphere is not excited by the sunlight (see e.g. fig. 2 of Bondonneau et al. 2021, which compare typical interference rates at the Nançay site). It is therefore optimal to observe when Jupiter is near opposition. Jupiter also has to be high enough in the sky ($\gtrsim$10°), to get more signal in the lobe of the antennas. A good approximation of the international LOFAR antennas effective area can be given by the following equation (see e.g. equation 3 of Grießmeier et al. 2021, fig. 1 of Bondonneau et al. 2020, 2021, and fig. 3 of Noutsos et al. 2015, for more precision):

$$A_{\rm eff} = A_{\rm eff_{max}} \cos^2 z, \tag{2}$$

where z is the zenith angle of the source and $A_{\rm eff_{max}}$ the maximal frequency-dependent effective area ($A_{\rm eff_{max}} = [3974.0–2516.0]$ m^2 in the range [15–30] MHz, see appendix B of van Haarlem et al. 2013, for more details).

2.3 Emission probability

Observations at very high temporal resolutions are very demanding in terms of disk space (∼7.6 GB per min of observation in the case of this study). We must therefore be sure that Jovian radio emission

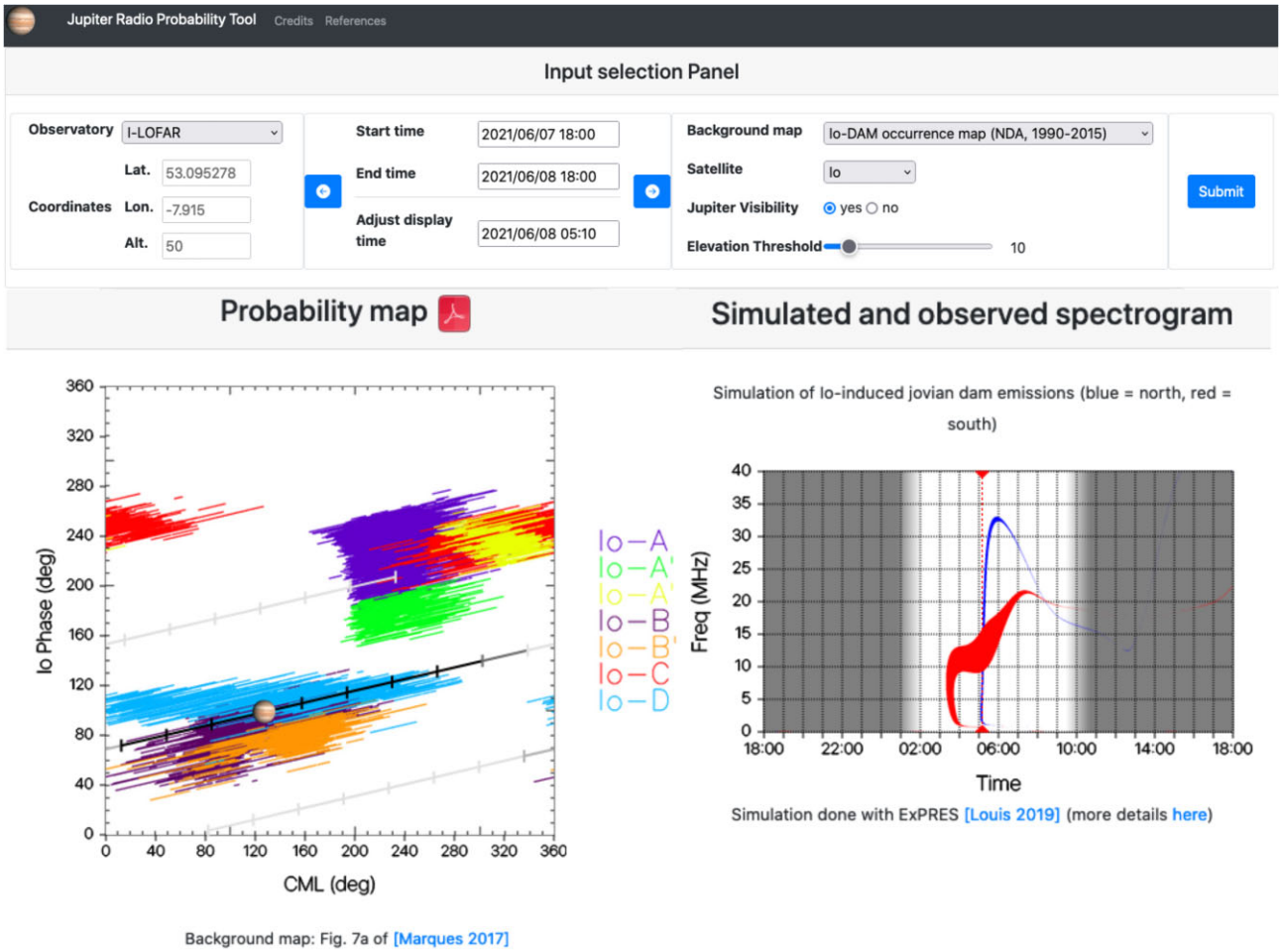

Figure 2. Example of results given by the online Jovian radio probability tool (https://jupiter-probability-tool.obspm.fr/). In this example, the station I-LOFAR has been chosen (*Observatory* entry; upper-left panel), for an observation between 2021 June 7 18:00 UTC and 2021 June 8 18:00 UTC (*Start time* and *End time* entries; upper-middle panel). The left-hand panel displays the occurrence probability map of Io-DAM emission (*Background map* entry; upper-right panel), in function of the Galilean moon position with respect to the observer (phase of the moon, *y*-axis) and the position of the observer (central meridian longitude, or CML, *x*-axis). The different colours correspond to different Io-DAM emissions (see text). The position of Jupiter in this map for the chosen time window is given by the black line (1 h tick). The miniature image of Jupiter gives the exact position for the time given in the *Adjust displayed time* entry (upper-middle panel). The right-hand panel displays the Exoplanetary and Planetary Radio Emission Simulator (ExPRES) simulation for a given moon (*Satellite* entry; upper-right panel). Blue corresponds to emission sources in the Northern hemisphere while red corresponds to emission sources in the Southern hemisphere. The thin red dashed line corresponds to the time given in the *Adjust displayed time* entry (upper-middle panel). The white area gives the time window in which Jupiter is visible above a certain elevation (*Elevation threshold* entry; upper-right panel).

will be observable during the time window when Jupiter is visible in the sky (at most 8 h per d, due to the rotation of the Earth).

To predict Jovian radio emissions, we use probability maps and simulations, that have been both gathered in an interactive online tool, called *Jupiter radio probability tool*.[1] An example is displayed in Fig. 2. This tool allows the user to choose (i) an observatory site from a pre-established list (*Observatory entry*; upper-left panel), or to enter the GPS coordinates (here 'I-LOFAR' is chosen as the observatory), (ii) a time window (*Start time* and *End time* entries; upper-middle panel), here from 2021 June 7 18:00 UTC to 2021 June 8 18:00 UTC), and finally (iii) a background map (upper-right entry) for the probability map (left-hand panel).

The probability maps (see Fig. 2; left-hand panel) show the position of the visible emissions as a function of the Jovian longitude of the observer (CML) and the phase of the Galilean moon (position of the satellite in the observer's frame, counted positively in the direction of rotation of the satellite, with the origin at the opposition). Fig. 2 (left-hand panel) displays the probability map for Io-DAM emission. The different colours correspond to different type of Io-DAM emission, that is associated to radio sources at different positions with respect to the observer (A: north-east of Jupiter, B: north-west, C: south-east, and D: south-west; see e.g. fig. 2 of Marques et al. 2017). The position of the observer in these maps is indicated by the position of the miniature image of Jupiter, with the black line displaying the location during the chosen time window (each tick is 1 h). Several probability maps have been published to predict auroral or Galilean moons induced DAM emissions such as Marques et al. (2017; the one displayed here), Zarka et al. 2017, 2018), Leblanc et al. (1993), and Louis et al. (2017b).

We also simulate the radio emission (see Fig. 2; right-hand panel), by using the ExPRES tool (Louis et al. 2019a, 2020b). This code is here used to produce simulations of the Jovian radio emission

[1] https://jupiter-probability-tool.obspm.fr/

linked to the interaction between Jupiter and the Galilean moons (Io, Europa, and Ganymede; see Louis, Cecconi & Loh 2020a for the data base), based on the CMI equations. More precisely, the simulations in this data base were produced using as input parameters the JRM09 magnetic field model (based on *in situ* measurements from the Juno mission; Connerney et al. 2018) and the Connerney, Acuna & Ness (1981) current sheet model to reproduce the magnetic field lines of Jupiter's magnetosphere, a 3 keV electron energy, and a loss cone electron distribution function. Using these standard parameters, the uncertainty for Io-DAM emission is expected to be well within a 2 h window (Louis et al. 2017a) around the predicted arc. Right-hand panel of Fig. 2 displays two arc-shape emissions related to Io-Jupiter interaction: The blue one is a northern emission (corresponding to an Io-B emission) while the red one is a southern emission (Io-D emission). The white area corresponds to the time when Jupiter is visible above an adjustable elevation (here above 10°), while the grey-shaded areas correspond to the time when Jupiter is below this elevation. The observer position indication, given in the left-hand panel (with the miniature image of Jupiter), is here represented by the thin vertical red dashed line (with the corresponding time in the *Adjust display time* entry; upper-middle panel).

Using this online tool, we are thus able to determine when the probability of observing Io-, Europa-, Ganymede-, or auroral-DAM emissions is the highest.

3 A FIRST CASE STUDY: OBSERVATION OF AN IO-DAM EMISSION

3.1 Origin of the observed emissions

As a first case study, and based on the prediction shown in Fig. 2, we observed Jupiter pre-dawn on 2021 June 8, between 04:00 and 07:00 UTC, with three different LOFAR stations: IE613 in Ireland, FR606 in France, and DE604 in Germany (see Fig. 1 for their respective position). In this study, the data were processed to obtain a time and frequency resolution of 81.92 μs and 12.2 kHz, respectively, and only the [8–40] MHz frequency range is displayed (40 MHz being the upper limit of the Jovian radio emissions).

Figs 3(a) and (b) display Stokes I (total intensity) and Stokes V (circular polarization) for IE613 observation. As predicted by the prediction tool (see Fig. 2), we detect an emission produced by the Io–Jupiter interaction. The emission is observed as multiple 'vertex early arc'-like feature and displays a negative circular (right-handed) polarization (see Stokes V parameter; Fig. 3b), which gives the information that this emission is an Io-B emission (coming from the north-west side of Jupiter as seen from the observer point of view, thus from the north-dawn side of Jupiter as seen from Earth). The main emission (emitted from the flux tube connected to Io) is observed from ∼05:00 to 05:30, while emission observed just before is produced in flux tubes connected to the tail upstream of Io (called secondary emission).

Figs A1 and A2 in the Supplementary Information display the four Stokes I, Q, U, and V parameters and the linear polarization L, showing that the emission is mostly exclusively circularly polarized, with almost zero polarization degrees for the Stokes parameters Q and U and a very low linear polarization intensity.

3.2 Probing the magnetic field amplitude at the sources of the emission

Since these radio emissions are produced via the CMI, and emitted at a frequency $f = f_{ce}$, we can probe the amplitude of the local magnetic field at the sources of the emission (see equation 1). In this case, the emissions are observed in the frequency range ∼[10–36] MHz (see Fig. 3a), therefore the local magnetic field at the sources of the observed radio emissions is in the range of ∼[3.6–12.9] G.

3.3 Determination of the parallel energy of the electrons producing the emission

Fig. 3c displays a 1 min zoom of Fig. 3a between 05:10:30 and 05:11:30. In this dynamic spectrum, we can see that the general arc shape of this emission has a detailed substructure. If we zoom-in even further, in a 10 s window (Fig. 3d), we then can clearly see that the Io emission is composed of many millisecond bursts, that present a negative drift (decreasing frequency with time).

This drift was interpreted by Ellis (1965, 1974) and Hess et al. (2007b), and confirmed by Hess et al. (2007a), as a radio source motion consistent with the electron adiabatic motion. In this model, the emission are produced along the field line at the local cyclotron frequency $f = f_{ce}$ via the CMI, by electrons reflected by the magnetic mirror effect (at a frequency called the mirror frequency f_{mirror}). The drift rate df/dt of the burst is therefore connected to the motion of the emitting electrons by the following equation (Hess et al. 2007b):

$$\frac{df}{dt} = \frac{df_{ce}}{dl}\frac{dl}{dt} = \frac{df_{ce}}{dl} v_{||}(f_{ce}), \tag{3}$$

with $v_{||}$ the emitting electron parallel velocity (chosen to be positive for upward electrons), and df_{ce}/dl the distance between sources (at different frequency f_{ce}) along the magnetic field line. f_{ce} being proportional to the magnetic field amplitude B (see equation 1), and using the JRM09 magnetic field model (based on *in situ* measurements of the magnetometer onboard Juno; Connerney et al. 2018), we can determine that in the frequency range [5–40] MHz, a difference of 1 MHz corresponds to a distance of about ∼1000 km.

This model of adiabatic motion of electrons remains valid as long as the first adiabatic invariant μ is conserved at all point along the magnetic field line:

$$\mu = \frac{m_e v_\perp^2}{2B} = \frac{|q| v_\perp^2}{4\pi f_{ce}} = \frac{|q| v^2}{4\pi f_{mirror}}, \tag{4}$$

where $v^2 = v_\perp^2 + v_{||}^2$ is the total energy. Therefore, as the particle moves towards increasing magnetic field, $v_\perp$ increases and $v_{||}$ decreases until the electrons reach there mirror point (where $v_{||} = 0$) before turning back.

The slope of the millisecond bursts then gives a direct indication of the direction of propagation of the electrons responsible for these emissions. Because the magnetic field strength decreases with altitude, we can therefore determine from the negative slope of these bursts (the emission frequency decreasing with time) that the electrons are propagating upward (from the planet to the higher altitudes).

Figs 3(f) and (h) show a 1 s zoom-in (between 05:10:37 and 05:10:38) in the [15–32] MHz frequency range of both Stokes I (intensity; panel f) and Stokes V (circular polarization; panel h) parameters. Superimposed on these two 1 s dynamic spectra are two examples of drifting millisecond bursts (orange lines), at two different frequency ranges.

The first drifting millisecond burst that is highlighted in Figs 3(f) and (h) extends from 30.83 to 22.32 MHz, from 05:10:37.274 to 05:10:37.673, thus displaying a drift of $df/dt \simeq -21.34$ MHz s^{-1}. Using equation 3, we can therefore determine that the electrons are propagating with a parallel velocity of $v_{||} \simeq 21340$ km s^{-1}. Using the

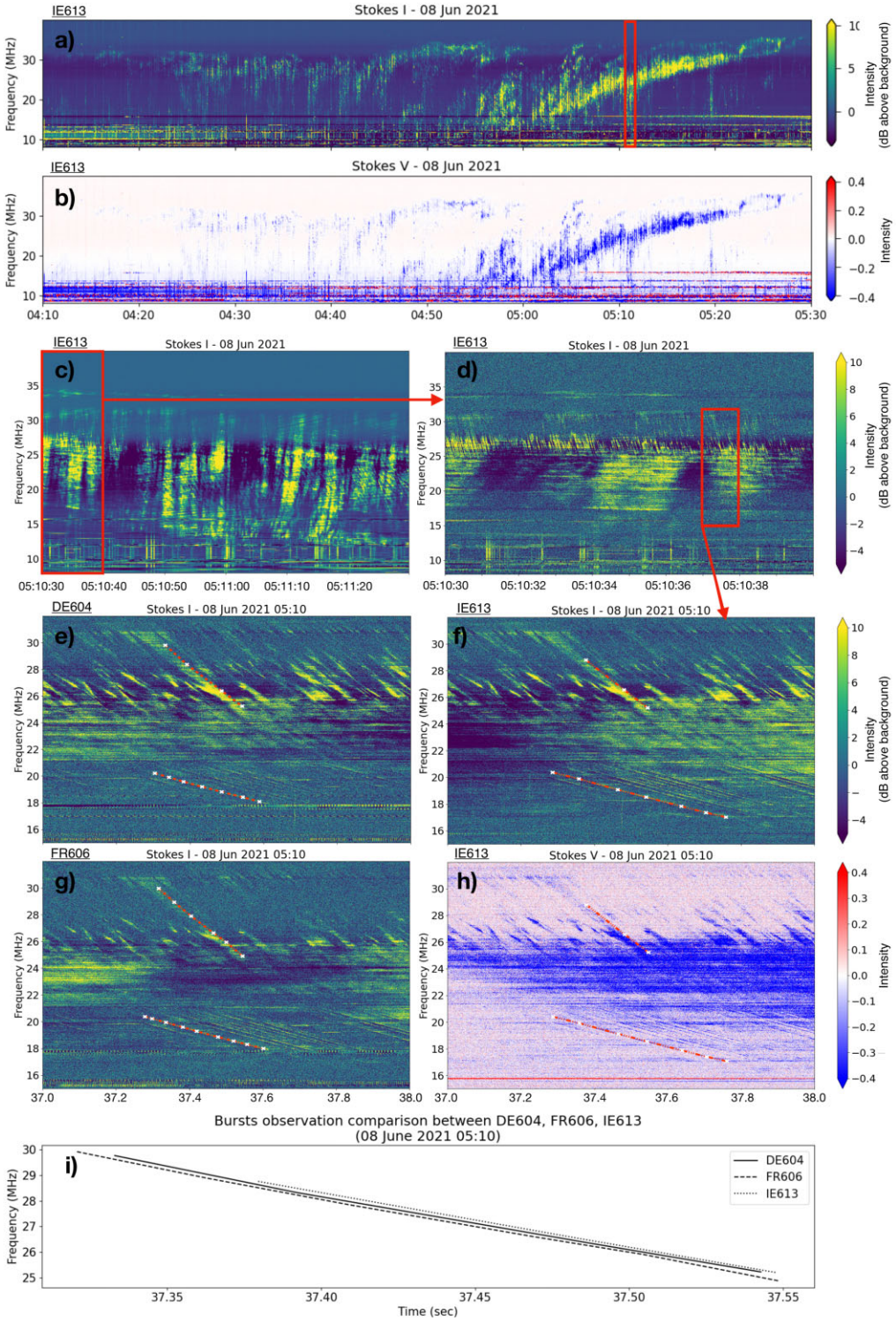

Figure 3. Observation of an Io-DAM emission, displayed in a time-frequency map (called *dynamic spectrum*), on different time windows, and for the stations IE613 (panels a–d, f, and h), DE604 (panel e), and FR606 (panel g). Panels (a) and (b), respectively, display Stokes I (corresponding to the intensity of the emission) and Stokes V (corresponding to the degree of circular polarization) parameters between 04:10 and 05:30 UTC on 2021 June 8. The observed 'vertex early arc'-like feature starting around 05:00 is the expected emission from the ExPRES code (see Fig. 2). Panels (c) and (d) are two zoom-in inside the red boxes, between c 05:10:30 and 05:11:30, and d 05:10:30 and 05:10:40, showing the data at a higher resolution. Panel f is a zoom of panel d of 1 s, between 05:10:37 and 05:10:38, in the range of [15–32] MHz, at the highest resolution use in this study, i.e. 81.92 μs in time and 12.2 kHz in frequency. Panels (e) and (g) are the equivalent of panel (f), displaying the data from the DE604 and FR606 stations, respectively. Panel h is the equivalent of panel f, displaying the Stokes V parameter (degrees of circular polarization). Panels (c)–(g) share the same intensity colour bar (displayed to the right of panels d and f). In panels (e)–(h), the red lines show example of drifting millisecond bursts. Panel i shows a comparison between the highest frequency bursts observed by the three stations (highlighted in panels e–h).

$E = 1/2 m_e v^2$ formula, we can determine that this drift corresponds to electrons with a parallel energy of $E_{||} \simeq 1.3$ keV.

The second drifting millisecond burst that is highlighted extends from 20.37 to 17.04 MHz, from 05:10:37.289 to 05:10:37.761, thus having a drift of $df/dt \simeq -7.06$ MHz s^{-1}. This corresponds to electrons propagating at a parallel velocity of $v_{||} \simeq 7060$ km s^{-1}, corresponding to a parallel energy of $E_{||} \simeq 0.14$ keV.

3.4 Observation of the Io-DAM emission by multiple LOFAR stations

Figs 3(e) and (g) display the observation acquired by the DE604 and FR606 stations during the same 10 s displayed in Fig. 3(f). The same bursts are highlighted.

Fig. 3(i) shows a zoom on the bursts at the highest frequencies, observed by the three stations (DE604 as a solid line, FR606 as a dashed line, and IE613 as a dotted line). A time shift of ∼8 ms is measured here, with FR606 seeing the burst before DE604 and then IE613. At that time (2021 June 8 05:10), Jupiter was located at 157°33′02.6″ in azimuth and 22°27′26.9″ in altitude in the sky. For an European observer, it means than Jupiter was located on the south section in the sky. Therefore in that case, it is more the south/north spreading of the three stations that matters (see Fig. 1). It is then expected that a radio emission from Jupiter will be observed first by FR606, then by DE604, and finally by IE613.

4 PERSPECTIVES

The observing method described in this article for observing Jupiter's radio emissions at high resolution could not be more timely. With the Juno mission we have *in situ* measurements for up to 2025, followed by the arrival of the Europa Clipper and JUICE missions in the late 2020s-early 2030s. The medium-resolution ground support has already existed for many years (with daily observation, e.g. Marques et al. 2017), and the addition of regular high-resolution measurements will allow comparative *in situ* and remote measurements. These results will be compared to simultaneous observation of the ultraviolet (UV) emission on Jupiter's atmosphere (by the Space Telescope Imaging Spectrograph instrument onboard the *Hubble Space Telescope* or by the UV spectrograph onboard the Juno mission; Gladstone et al. 2017), or to X-ray auroral observation (using e.g. *Chandra* and *XMM*). This once-in-a-generation combination of high fidelity *in situ* and remote sensing measurement will allow us to make breakthrough on several key scientific questions for Jupiter.

We have demonstrated the predictive power of the ExPRES simulations and the probability maps (gathered on the Jupiter radio probability tool), the observing capability of the LOFAR network, and the data analysis methods enabled by software support (e.g. REALTA; Murphy et al. 2021) and domain knowledge (e.g. the search for millisecond bursts in the high-resolution data stream). We now highlight several future avenues for the exploitation of this rich LOFAR data set.

The millisecond bursts which we have presented here have the potential to reveal important information about the nature of electron acceleration regions at Jupiter. Specifically, examination of the drifting of the bursts can tell us about the electron population energy that gives rise to this emission, in particular on the differences in electron energies as a function of frequency, but also by comparing the energies of the electrons in the main (linked to Io itself) and secondary (linked to Io's tail) emissions. Particular attention will be paid to abrupt changes in the drift rate of the millisecond bursts, which will reveal electric potential drops along these field lines, and thus acceleration regions of the electrons. In order to conduct robust statistical examination of these bursts with future larger LOFAR observations, we plan to apply automatic detection algorithms (e.g. Hess et al. 2007b) which will enable examination of the bursts over an extensive frequency range.

Secondly, we plan to unlock the full power of the radio emissions as a tool to provide information about the nature of the radio source locations themselves. We plan to do this by combining the latest Jovian magnetic field (JRM33; Connerney et al. 2022) and current sheet (Connerney et al. 2018) models, with sophisticated inter-station interferometry. The addition of the IE613 station to the international LOFAR radio telescope increases the longest baseline by more than 300 km (∼1515 km from UK608 to PL612 stations, now ∼1883 km between IE613 and PL612 stations; see Fig. 1). Since, to first order, the angular resolution[2] is proportional to λ (the observing wavelength) over the baseline length L (distance between the stations), the addition of IE613 station increases the angular resolution from 3.268 to 2.629 arcsec at 10 MHz, and from 0.934 to 0.751 arcsec at 35 MHz. This will enable us to estimate more precisely the location of sources in longitude, latitude, and altitude. When this information is combined with *in situ* Juno measurements, it will represent an extremely powerful probe of the response of the Jovian radio sources to magnetospheric dynamics.

Thirdly, we plan to use the radio emissions to reveal the electron density along Io's trajectory. In order to do this we will utilize the property that the CMI perturbation is moving at the Alfvén speed:

$$v_A = B/\sqrt{\mu_0 \rho}, \tag{5}$$

(with B the local magnetic field amplitude and ρ the local electron density), and that Io is surrounded by a dense plasma torus (produced by its volcanic activity which releases about one tonne of plasma per second). This leads to a difference in longitude (called *lead angle*; see Fig. 4) between the Io IFT (connected to Io) and the Io AFT (where the sources of the main emission are). Once the exact locations of the sources are known (e.g. by interferometry, or using instantaneous observations of the Io-induced UV emissions), we will be able to obtain the longitude of the AFT, and to determine the lead angle in longitude between the IFT and the AFT. Knowing this will give the possibility to estimate the electron density inside the Io torus using equation 5.

Finally, once the AFT position is known, it will also make it possible to determine the beaming angle θ of the emitting cone, as well as determine the electron energy in a second way (the first being using the drift rate of the millisecond bursts), by using the theoretical formula of the CMI:

$$\theta = \arccos\left(\frac{v/c}{\sqrt{1 - f_{ce}/f_{ce_{max}}}}\right), \tag{6}$$

with v the total electron velocity, f_{ce} the local electron cyclotron frequency, and $f_{ce_{max}}$ the maximal electron cyclotron frequency at the footprint of the magnetic field lines.

All these studies are beyond the scope of this paper describing the methodology, and will be the focus of a future scientific work. The methodology and study perspectives described here can later be applied to new observations of Jovian radio emissions induced by Io, but also by Ganymede or Europa, or Jovian auroral radio emissions.

[2] https://science.astron.nl/telescopes/lofar/lofar-system-overview/observing-modes/lofar-imaging-capabilities-and-sensitivity/

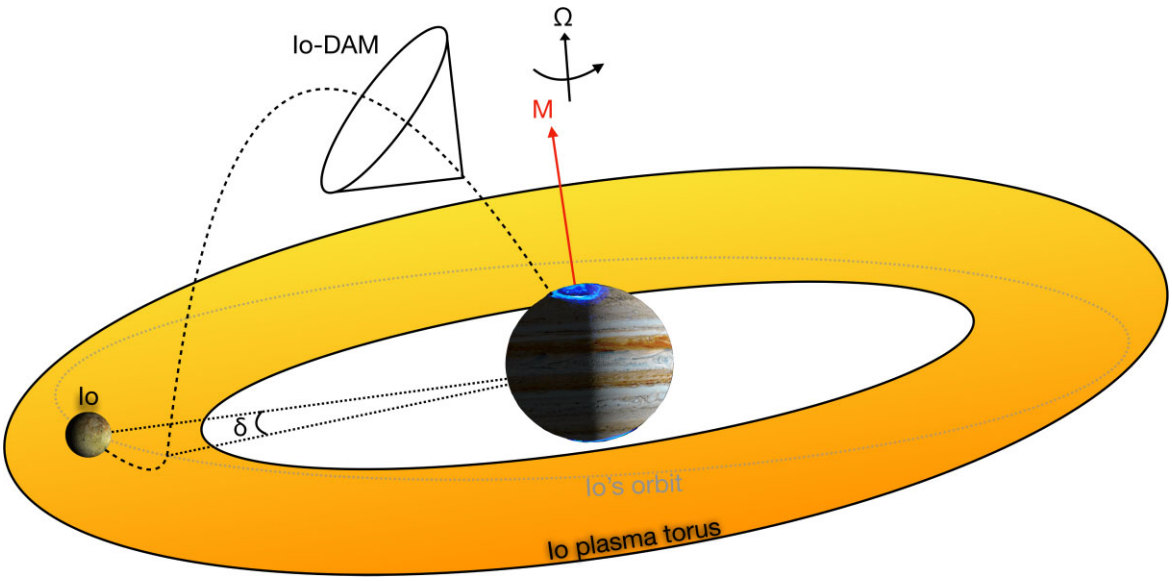

Figure 4. Sketch of the Io–Jupiter interaction. The shaded-grey-dotted line represents the orbit of Io, while the Io torus is represented in yellow (where the density is higher than elsewhere in the Jovian magnetosphere). The active magnetic flux tube (AFT) where the Io-DAM emission occurred is displayed as the black-dashed line. The Io-DAM emission is beamed along the edges of the hollow cone. The black-dotted lines represent the longitude of the instantaneous magnetic flux tube (IFT) connected to Io and the active magnetic field line, separated by the lead angle δ. The red arrow represents the direction of the magnetic field axis, while the black arrows represent the rotation axis and the sense of rotation of Jupiter.

ACKNOWLEDGEMENTS

This paper is using data obtained with the DE604, FR606, and IE613 stations of the *International LOFAR Telescope*, constructed by ASTRON, during station-owners time. German DE604 station is funded by the Leibniz-Institut für Astrophysik Potsdam. These observations were carried out in the stand-alone GLOW mode (German LOng-Wavelength array), which is technically operated and supported by the Max-Planck-Institut für Radioastronomie, the Forschungszentrum Jülich, and Bielefeld University. Nançay Radio Observatory FR606 station is operated by Paris Observatory, associated with the French Centre National de la Recherche Scientifique and Université d'Orléans. Irish IE613 station received funding from Science Foundation Ireland (SFI), the Department of Jobs Enterprise and Innovation (DJEI). The REALTA backend used at IE613 station is funded by SFI and Breakthrough Listen. The Irish-LOFAR consortium consists of Trinity College Dublin, University College Dublin, Athlone Institute for Technology, Armagh Observatory and Planetarium (supported through funding from the Department for Communities of the N. Ireland Executive), Dublin City University, Dublin Institute for Advanced Studies, National University of Ireland Galway, and University College Cork. The authors thank S. Aicardi for developing https://jupiter-probability-tool.obspm.fr. CKL and CMJ's work at DIAS is supported by the Science Foundation Ireland Grant 18/FRL/6199. PCM and DM are supported by Government of Ireland Studentships from the Irish Research Council (IRC). DÓF is supported by a Government of Ireland Postdoctoral Fellowship from the IRC (GOIPD/2020/145). We acknowledge support and operation of the GLOW network, computing and storage facilities by the FZ-Jülich, the MPIfR, and Bielefeld University, and financial support from BMBF D-LOFAR III (grant 05A14PBA) and D-LOFAR IV (grant 05A17PBA), and by the states of Nordrhein-Westfalia and Hamburg.

DATA AVAILABILITY

The LOFAR data presented in this article are accessible at doi: 10.5281/zenodo.6460746a (Louis et al. 2022), and the Python routine to process them at doi: 10.5281/zenodo.6470741 (Louis 2022). The Jupiter probability tool is accessible at the following address: https://jupiter-probability-tool.obspm.fr/. The ExPRES simulations used in the Jupiter probability tool are accessible at doi: 10.25935/kpge-zb59 (Louis et al. 2020a).

REFERENCES

Bigg E. K., 1964, Nature, 203, 1008
Boischot A. et al., 1980, Icarus, 43, 399
Bondonneau L., Grießmeier J. M., Theureau G., Bilous A. V., Kondratiev V. I., Serylak M., Keith M. J., Lyne A. G., 2020, A&A, 635, A76
Bondonneau L. et al., 2021, A&A, 652, A34
Braude S. I., Men A. V., Sodin L. G., 1978, Antenny, 26, 3
Burke B. F., Franklin K. L., 1955, J. Geophys. Res., 60, 213
Connerney J. E. P., Acuna M. H., Ness N. F., 1981, J. Geophys. Res., 86, 8370
Connerney J. E. P. et al., 2018, Geophys. Res. Lett., 45, 2590
Connerney J. E. P. et al., 2022, J. Geophys. Res. (Planets), 127, e07055
Ellis G. R. A., 1965, Radio Sci., 69D, 1513
Ellis G. R. A., 1974, Proc. Astron. Soc. Aust., 2, 236
Gladstone G. R. et al., 2017, Space Sci. Rev., 213, 447
Grießmeier J.-M., Smith D. A., Theureau G., Johnson T. J., Kerr M., Bondonneau L., Cognard I., Serylak M., 2021, A&A, 654, A43
Hess S., Mottez F., Zarka P., 2007a, J. Geophys. Res. (Space Phys.), 112, A11212
Hess S., Zarka P., Mottez F., 2007b, Planet. Space Sci., 55, 89
Hess S., Cecconi B., Zarka P., 2008, Geophys. Res. Lett., 35, L13107
Hirshfield J. L., Bekefi G., 1963, Nature, 198, 20
Kaiser M. L., Zarka P., Kurth W. S., Hospodarsky G. B., Gurnett D. A., 2000, J. Geophys. Res., 105, 16053

Leblanc Y., Gerbault A., Denis L., Lecacheux A., 1993, A&AS, 98, 529
Louarn P. et al., 2017, Geophys. Res. Lett., 44, 4439
Louis C. K., 2022, CorentinLouis/ILOFAR: LOFAR Data Processing Pipeline for Jupiter Observations (v1.1.0), Zenodo, available at https://doi.org/10.5281/zenodo.6470741
Louis C., Lamy L., Zarka P., Cecconi B., Hess S. L. G., Bonnin X., 2017a, in Fischer G., Mann G., Panchenko M., Zarka P., eds, Planetary Radio Emissions VIII. Aust. Acad. Sci. Press, Vienna, p. 59
Louis C. K., Lamy L., Zarka P., Cecconi B., Hess S. L. G., 2017b, J. Geophys. Res. (Space Phys.), 122, 9228
Louis C. K. et al., 2017c, Geophys. Res. Lett., 44, 9225
Louis C. K., Hess S. L. G., Cecconi B., Zarka P., Lamy L., Aicardi S., Loh A., 2019a, A&A, 627, A30
Louis C. K., Prangé R., Lamy L., Zarka P., Imai M., Kurth W. S., Connerney J. E. P., 2019b, Geophys. Res. Lett., 46, 11606
Louis C. K., Cecconi B., Loh A., 2020a, ExPRES Jovian Radio Emission Simulations Data Collection (Version 01), PADC, Paris, France
Louis C. K., Hess S. L. G., Cecconi B., Zarka P., Lamy L., Aicardi S., Loh A., 2020b, maserlib/ExPRES: Version 1.1.0, Zenodo/PADC, available at https://doi.org/10.5281/zenodo.4292002
Louis C. K., Louarn P., Allegrini F., Kurth W. S., Szalay J. R., 2020c, Geophys. Res. Lett., 47, e90021
Louis C. K. et al., 2022, LOFAR IE613/DE604/FR606 Observations of Io-Decametric Radio Emissions, Zenodo, available at https://doi.org/10.5281/zenodo.6460746
Marques M. S., Zarka P., Echer E., Ryabov V. B., Alves M. V., Denis L., Coffre A., 2017, A&A, 604, A17
Murphy P. C. et al., 2021, A&A, 655, A16
Noutsos A. et al., 2015, A&A, 576, A62
Pritchett P. L., 1986, Phys. Fluids, 29, 2919
Treumann R. A., 2006, A&A, 13, 229
Twiss R. Q., 1958, Aust. J. Phys., 11, 564
van Haarlem M. P. et al., 2013, A&A, 556, A2
van Straten W., Bailes M., 2011, Publ. Astron. Soc. Aust., 28, 1
Wu C. S., Lee L. C., 1979, ApJ, 230, 621
Zarka P., 1998, J. Geophys. Res., 103, 20159
Zarka P., 2004, Planet. Space Sci., 52, 1455
Zarka P., Farges T., Ryabov B. P., Abada-Simon M., Denis L., 1996, Geophys. Res. Lett., 23, 125
Zarka P., Girard J. N., Tagger M., Denis L., 2012, in Boissier S., de Laverny P., Nardetto N., Samadi R., Valls-Gabaud D., Wozniak H., eds, SF2A-2012: Proceedings of the Annual meeting of the French Society of Astronomy and Astrophysics. SF2A, Paris, France, p. 687
Zarka P. et al., 2015, in 2015 International Conference on Antenna Theory and Techniques (ICATT). IEEE, Kharkiv, Ukraine
Zarka P., Marques M. S., Louis C., Ryabov V. B., Lamy L., Echer E., Cecconi B., 2017, in Fischer G., Mann G., Panchenko M., Zarka P., eds, Planetary Radio Emissions VIII. Aust. Acad. Sci. Press, Vienna, p. 45
Zarka P., Marques M. S., Louis C., Ryabov V. B., Lamy L., Echer E., Cecconi B., 2018, A&A, 618, A84

APPENDIX A: FULL STOKES PARAMETERS AND LINEAR POLARIZATION OF IE613 OBSERVATION

Figs A1 and A2 display the four Stokes parameters (I, Q, U, and V) and the linear polarization $L = \sqrt{Q^2 + U^2}$ for the IE613 observation between 04:10 and 05:40 (Fig. A1) and between 05:10:37 and 05:10:38 at the highest resolution available. First and fourth panels of Figs A1 and A2 display the Stokes I and V parameters (same plots as Figs 3a, b, f, and h, respectively), while the second and third panels of Figs A1 and A2 display the Stokes Q and U parameters. Finally, the fifth panel of Figs A1 and A2 displays the intensity of linear polarization *L*.

One can clearly see on these two figures that Stokes Q and U parameters are quasi-null compared to Stokes V values (the scale of the colour bar is the same between the Stokes parameters Q, U, and V to facilitate comparison), and that the intensity of linear polarization peaks at <0.5 for the main emission (in Fig. A1, secondary emissions are almost not visible in linear polarization), showing that the observed emissions are mainly circularly polarized.

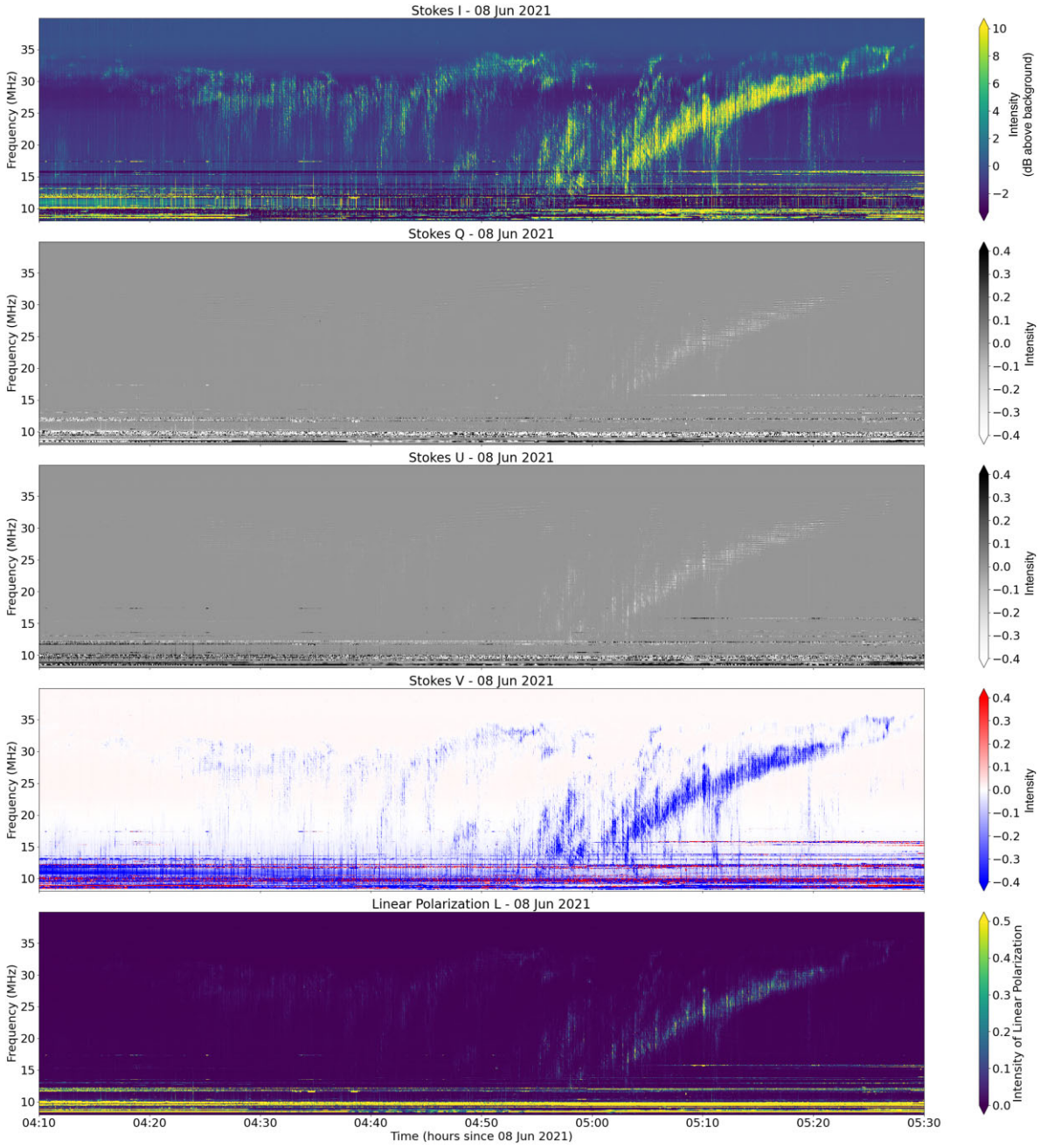

Figure A1. Full Stokes IQUV (first four panels) parameters and linear polarization $L = \sqrt{Q^2 + U^2}$ of the IE613 observation displayed in Figs 3(a) and (b), between 04:10 and 05:30.

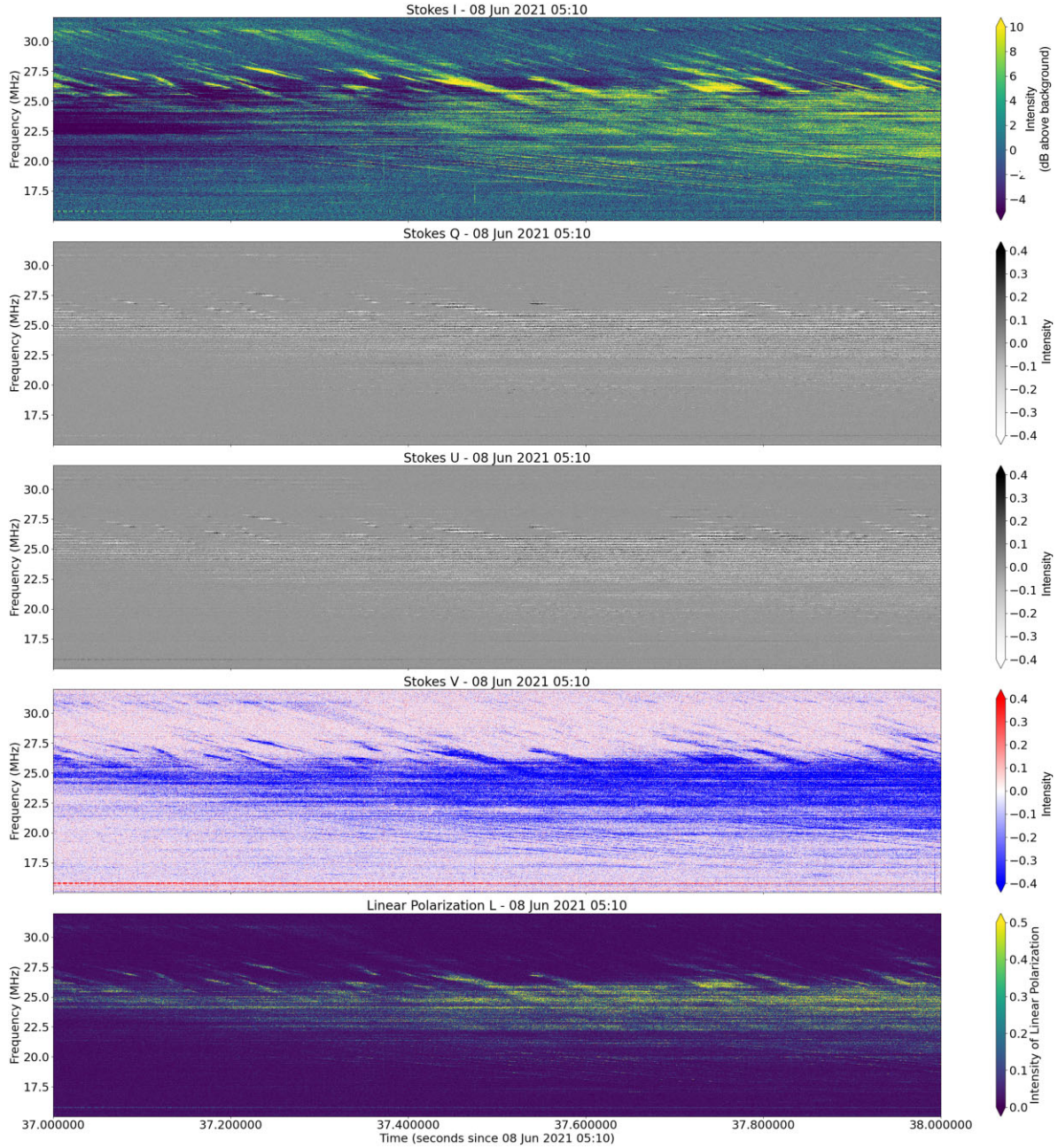

Figure A2. Full Stokes IQUV (first four panels) parameters and linear polarization $L = \sqrt{Q^2 + U^2}$ of the IE613 observation displayed in Figs 3(f) and (h), between 05:10:37 and 05:10:38.

This paper has been typeset from a TEX/LATEX file prepared by the author.